Supplementary Information

High-Performance Electronic and Thermoelectric Devices Based on Ferroelectric In_2Se_3/Antimonene Heterostructure

Anwar Ali [a,b,c], Wen Zhang [d], Iqtidar Ahmad [a], Bin Lu [b,c], F. F. Al-Harbi [e], Ismail Shahid [f,*]

[a] College of Physics and Optoelectronic Engineering, Shenzhen University, Shenzhen 518060, P.R China

[b] School of Microelectronics, Northwestern Polytechnical University, Xi'an 710072, Shaanxi, China

[c] Research & Development Institute of Northwestern Polytechnical University, Shenzhen 518057, China

[d] Key Laboratory of Quantum Materials and Devices of Ministry of Education, School of Physics, Southeast University, Nanjing, 211189, China

[e] Department of Physics, College of Science, Princess Nourah bint Abdulrahman University, P. O. Box 84428, Riyadh 11671, Saudi Arabia

[f] Key Laboratory of Ocean Energy Utilization and Energy Conservation of Ministry of Education, School of Energy and Power Engineering, Dalian University of Technology, Dalian 116024, China

[*]Corresponding author: Email: docismailshahid@gmail.com (I. Shahid)

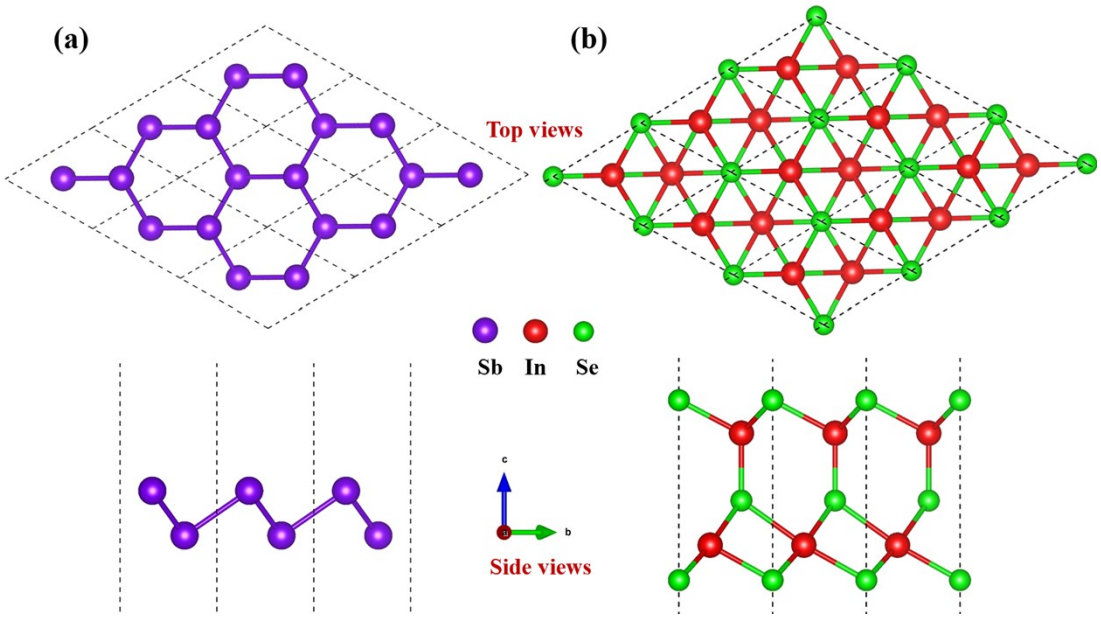

Fig. S1. Top and side views atomic structures of (a) Sb and (b) In_2Se_3 monolayers.

Table S1. The optimized lattice parameters (a in Å), electronic band gaps (E_g in eV), Seebeck coefficient (S in μV/K), lattice thermal conductivity (κ_l in $WK^{-1}m^{-1}$), and figure of merit (ZT) for the In_2Se_3/Sb heterostructures and their monolayers. Previously available experimental and theoretical results are also listed for comparison.

Systems	a	E_g^{PBE}	E_g^{HSE06}	E_g^{Experi}	S	κ_l	ZT
Sb	4.07	1.24	1.79	-	-	-	-
	4.09 [1]	1.22 [1]	1.75 [2]	1.60 [3]	800 [4]	15.1 [5]	0.8 [4]
In_2Se_3	4.10	0.79	1.49	-	-	-	-
	4.06 [6]	0.80 [6]	1.52 [6]	1.64 [7]	500 [8]	4.00 [8]	0.28 [8]
In_2Se_3/Sb-P↑	4.08	-	1.12	-	2030	1.10	3.60
In_2Se_3/Sb-P↓	4.09	-	0.20	-	394	0.77	2.00

Table S2. Binding energy (E_i in eV) for possible configurations (i=a, b, c, d), interlayer spacing (d_o in Å), optimized lattice parameters (a in Å), band gaps (E_g in eV) for In_2Se_3/Sb-P↑ and In_2Se_3/Sb-P↓ heterostructures.

Heterojunctions	In_2Se_3/Sb-P↑	In_2Se_3/Sb-P↓
E_a	-0.26	-0.30
d_o	3.20	3.01
E_b	-0.27	-0.32
d_o	3.07	2.89
E_c	-0.26	-0.31
d_o	3.18	3.00
a	4.08	4.09
E_g (HSE06)	1.12	0.20

Table S3. Electron/hole mobility (μ_{2D}), effective mass (m*), in-plane stiffness (C_{2D}) and deformation potential constant (E_{DP}) of In_2Se_3/Sb-P↑ an In_2Se_3/Sb-P↓ heterostructures.

Systems	Carrier	E_{DP} (eV)	C_{2D} (Nm^{-1})	m^* (m_e)	μ_{2D} ($cm^2V^{-1}S^{-1}$)
In_2Se_3/Sb-P↑	e	2.60	127	0.42	1518
	h	2.20	127	1.00	374
In_2Se_3/Sb-P↓	e	3.00	125	0.49	825
	h	2.35	125	1.02	310

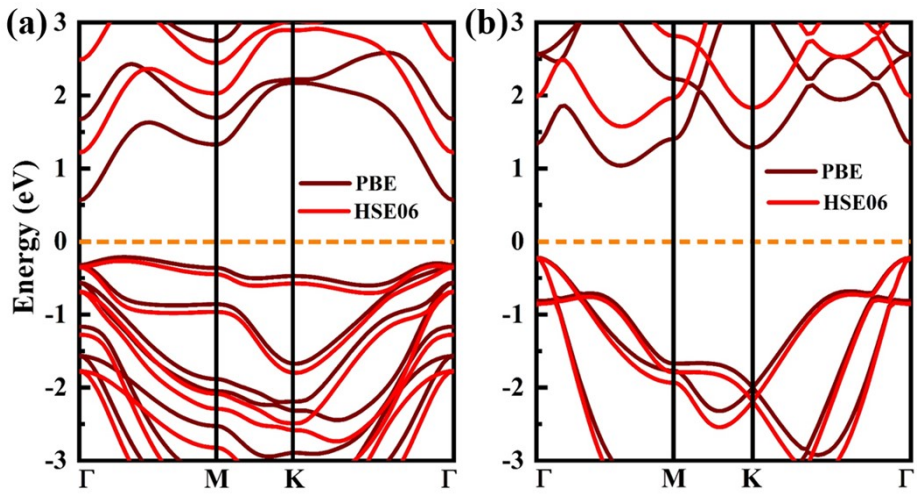

Fig. S2. Electronic band structures of (a) In_2Se_3 (b) Sb monolayers.

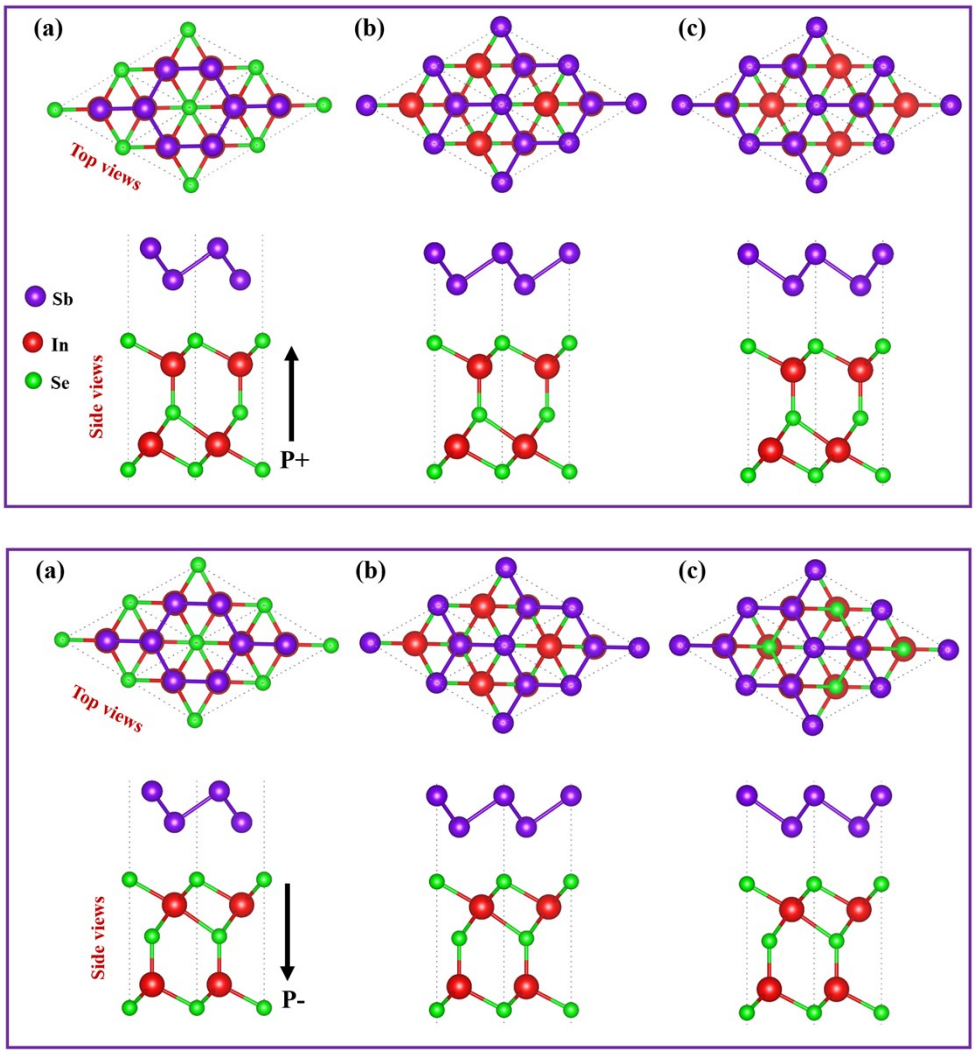

Fig. S3. Possible stacking of In_2Se_3/Sb-P↑ and In_2Se_3/Sb-P↓ heterostructures.

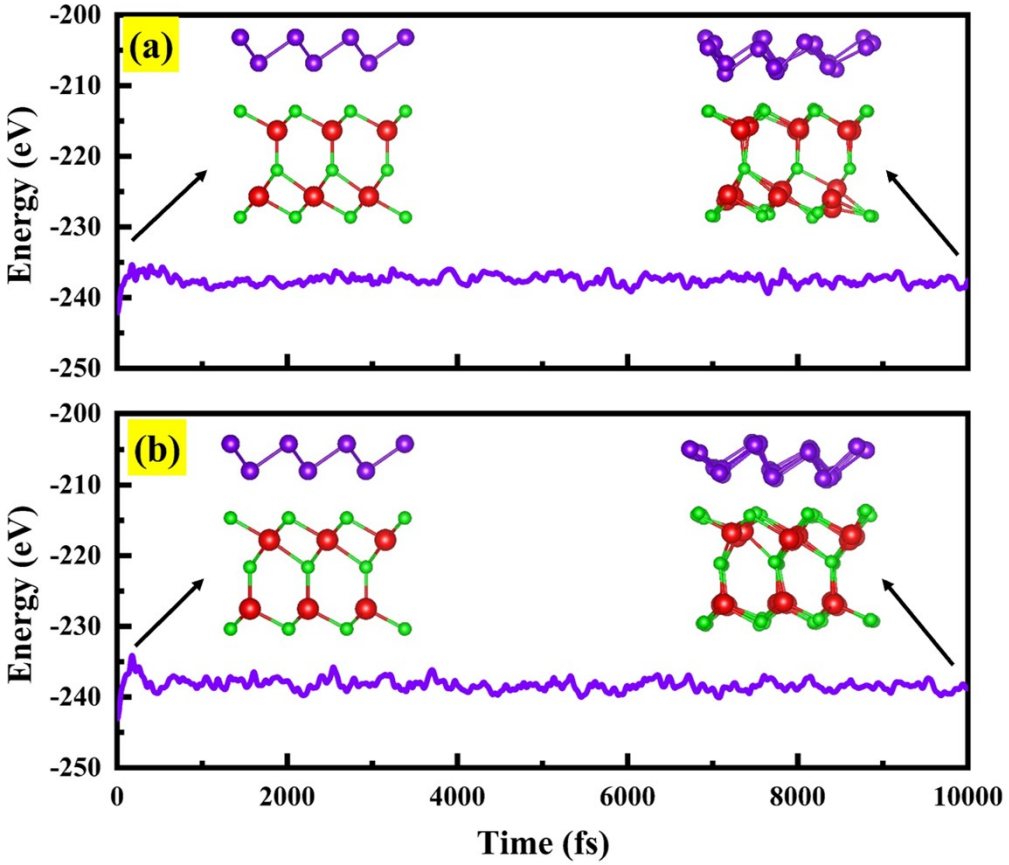

Fig. S4. Calculated AIMD simulations of (a) In_2Se_3/Sb-P↑ and (b) In_2Se_3/Sb-P↓ heterostructures at 700K.

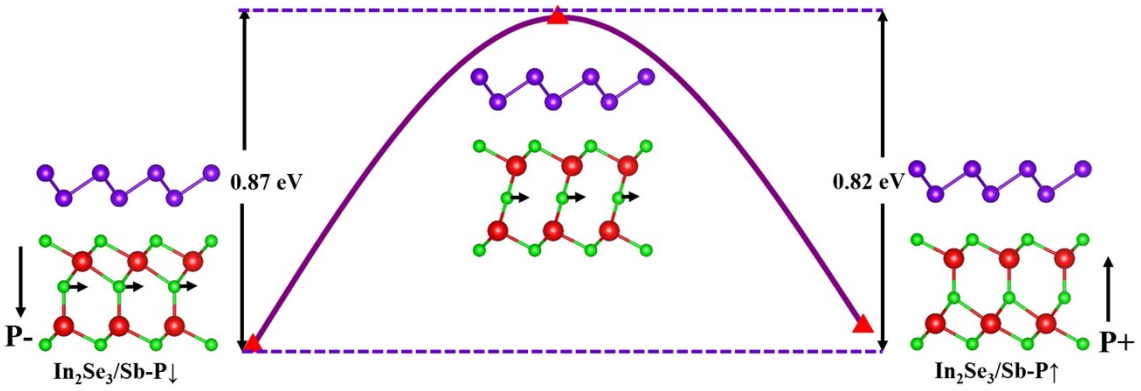

Fig. S5. Kinetic pathways of the polarization reversal processes in In_2Se_3/Sb heterostructure.

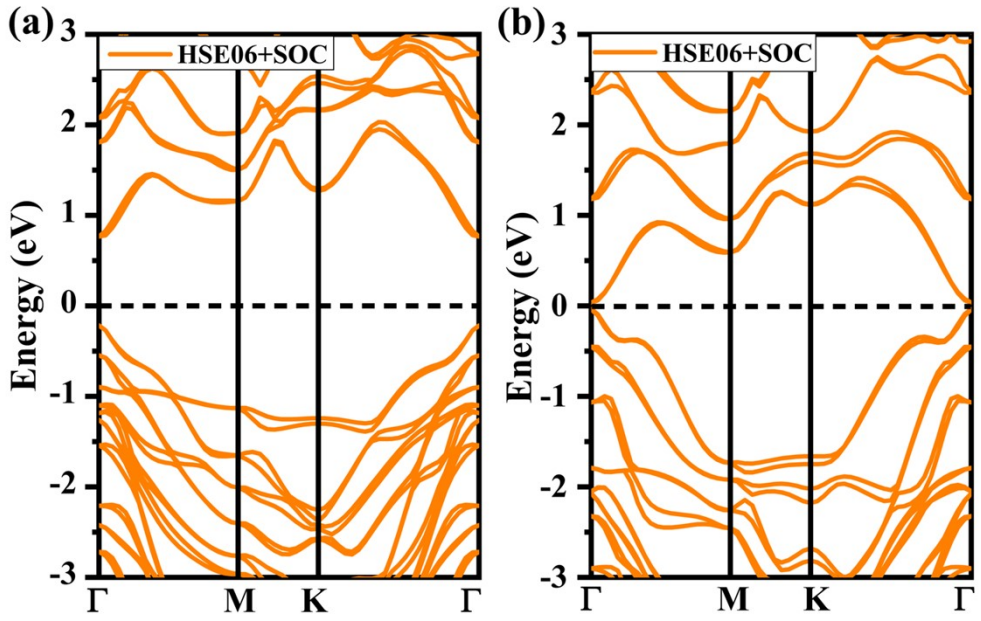

Fig. S6. Electronic band structures of (a) In_2Se_3/Sb-P↑ and (b) In_2Se_3/Sb-P↓ heterostructures.

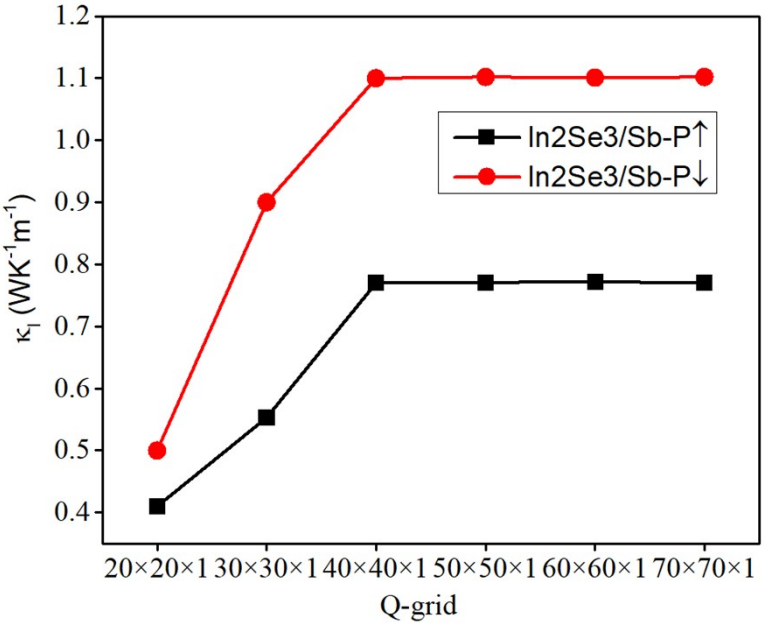

Fig. S7. The convergence test results of the phonon thermal conductivity at 300 K for In_2Se_3/Sb-P↑ and In_2Se_3/Sb-P↓ heterostructures.

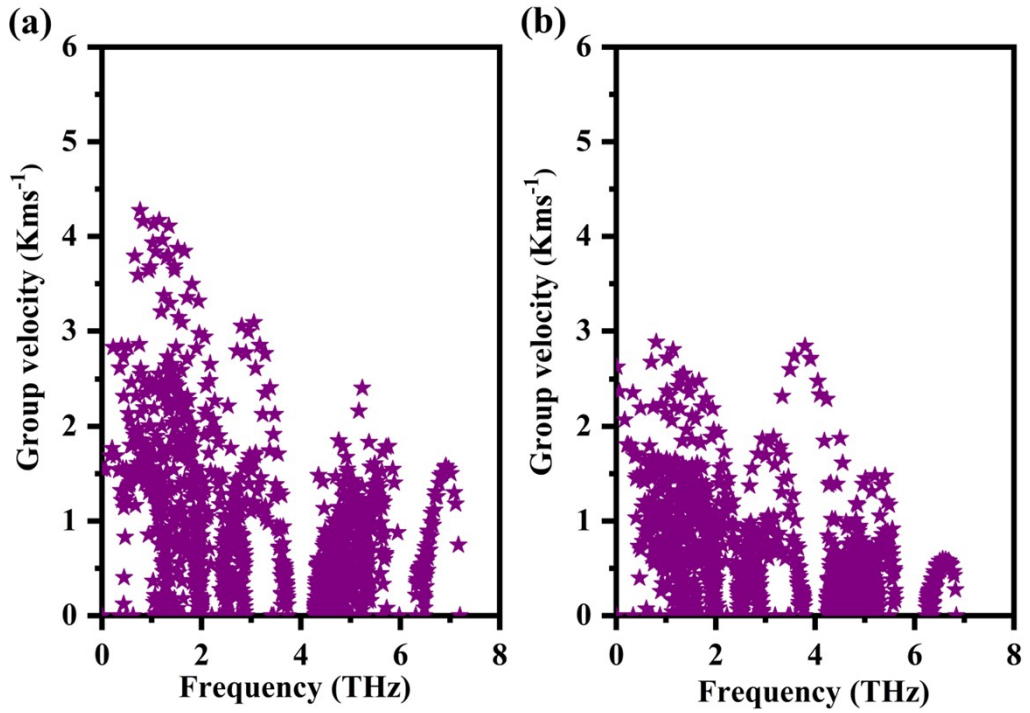

Fig. S8. Calculated phonon group velocity for (a) In_2Se_3/Sb-P↑ and (b) In_2Se_3/Sb-P↓ heterostructures.

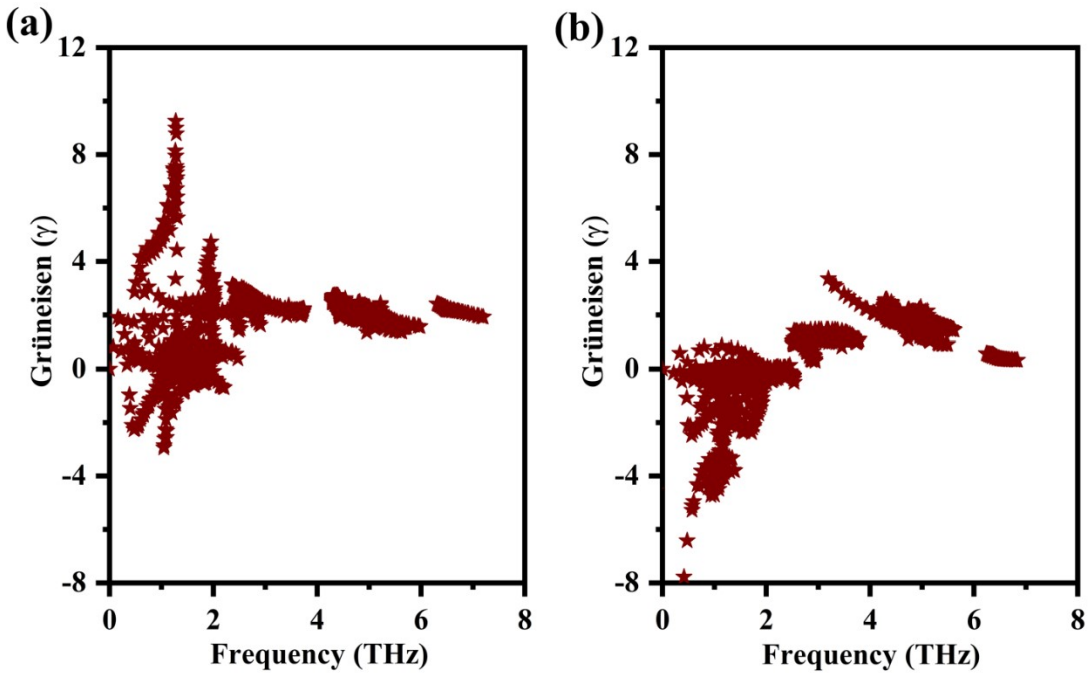

Fig. S9. Grüneisen parameters with respect to the frequency for (a) In_2Se_3/Sb-P↑ and (b) In_2Se_3/Sb-P↓ heterostructures.

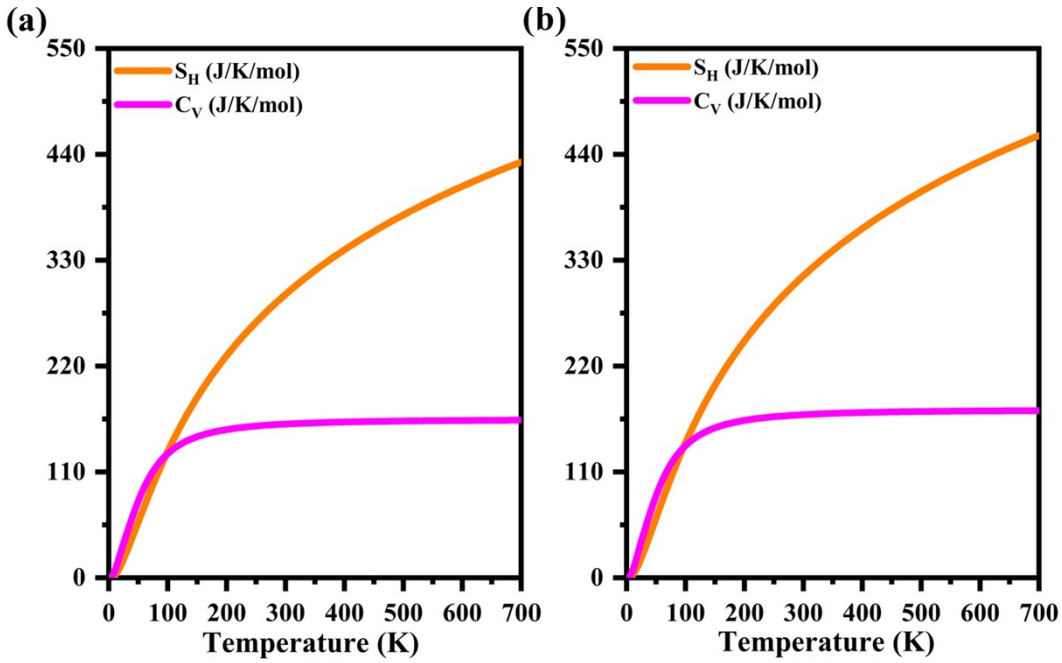

Fig. S10. Calculated entropy and heat capacity for (a) In_2Se_3/Sb-P↑ and (b) In_2Se_3/Sb-P↓ heterostructures.

References

1 Z. Zhang, Y. Zhang, Z. Xie, X. Wei, T. Guo, J. Fan, L. Ni, Y. Tian, J. Liu and L. Duan, Tunable electronic properties of an Sb/InSe van der Waals heterostructure by electric field effects, *Phys. Chem. Chem. Phys.*, 2019, **21**, 5627–5633.

2 Y. Cheng, L. Li, L. Li, Y. Zhang, L. Wang, L. Wang, Z. Zhang and Y. Gao, Linear regulation of electrical characteristics of InSe/Antimonene heterojunction via external electric field and strain, *Surfaces and Interfaces*, 2021, **23**, 101014.

3 P. Ares, F. Aguilar-Galindo, D. Rodríguez-San-Miguel, D. A. Aldave, S. Díaz-Tendero, M. Alcamí, F. Martín, J. Gómez-Herrero and F. Zamora, Mechanical Isolation of Highly Stable Antimonene under Ambient Conditions, *Adv. Mater.*, 2016, **28**, 6332–6336.

4 S. Sharma, S. Kumar and U. Schwingenschlögl, Arsenene and Antimonene: Two-Dimensional Materials with High Thermoelectric Figures of Merit, *Phys. Rev. Appl.*, 2017, **8**, 44013.

5 S. Wang, W. Wang and G. Zhao, Thermal transport properties of antimonene: an ab initio study, *Phys. Chem. Chem. Phys.*, 2016, **18**, 31217–31222.

6 Q. Lu, L.-L. Zhang, T.-T. Xu, B.-Y. Zhang and W.-J. Gong, Highly efficient photocatalytic water

splitting in direct Z-scheme α-In2Se3/Are van der Waals heterostructures, *Surfaces and Interfaces*, 2023, **36**, 102608.

7 F. Lyu, Y. Sun, Q. Yang, B. Tang, M. Li, Z. Li, M. Sun, P. Gao, L.-H. Ye and Q. Chen, Thickness-dependent band gap of α-In2Se3: from electron energy loss spectroscopy to density functional theory calculations, *Nanotechnology*, 2020, **31**, 315711.

8 X. Yang and A. Chen, Thermoelectric properties of ferroelectric α-In2X3 (X = S, Se, Te) monolayers: A first-principles study, *Mater. Today Commun.*, 2024, **41**, 111096.